LANGMUIR

Article

pubs.acs.org/Langmuir

Coating Graphene Oxide with Lipid Bilayers Greatly Decreases Its Hemolytic Properties

Bingen G. Monasterio,[†,‡] Beatriz Alonso,[∥] Jesús Sot,[†,‡] Aritz B. García-Arribas,[†,‡] David Gil-Cartón,[§] Mikel Valle,[§] Amaia Zurutuza,[∥] and Félix M. Goñi*[,†,‡]

[†]Instituto Biofísika (CSIC, UPV/EHU) and [‡]Departamento de Bioquímica, Universidad del País Vasco, Leioa 48940, Spain
[§]Structural Biology Unit, Center for Cooperative Research in Biosciences, CIC bioGUNE, Derio 48160, Spain
[∥]Graphenea, San Sebastian 20009, Spain

Supporting Information

ABSTRACT: Toxicity evaluation for the proper use of graphene oxide (GO) in biomedical applications involving intravenous injections is crucial, but the GO circulation time and blood interactions are largely unknown. It is thought that GO may cause physical disruption (hemolysis) of red blood cells. The aim of this work is to characterize the interaction of GO with model and cell membranes and use this knowledge to improve GO hemocompatibility. We have found that GO interacts with both neutral and negatively charged lipid membranes; binding is decreased beyond a certain concentration of negatively charged lipids and favored in high-salt buffers. After this binding occurs, some of the vesicles remain intact, while others are disrupted and spread over the GO surface. Neutral membrane vesicles tend to break down and extend over the GO, while vesicles with negatively charged membranes are mainly bound to the GO without disruption. GO also interacts with red blood cells and causes hemolysis; hemolysis is decreased when GO is previously coated with lipid membranes, particularly with pure phosphatidylcholine vesicles.

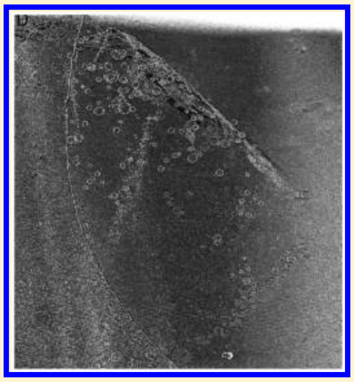

INTRODUCTION

Nanomaterials have attracted widespread interest particularly in relation to their biological applications. They have been used as biosensors,[1,2] in gene and drug trafficking,[3] as DNA probes,[4] in tissue engineering,[5,6] as heat-mediated antitumor agents,[7] for separation and purification processes,[8] for improved contrast in cell imaging,[9] or in phagocytic studies[10] among others. An interesting area is the development and use of nanomaterial-based vaccines and nanodrugs.[11−13]

Graphene is the name given to a highly packed 6-carbon ring, planar monolayer nanomaterial.[14] For the last 10 years, graphene and its derivatives graphene oxide (GO) and reduced graphene oxide (rGO) have been studied in the context of a large number of applications, especially due to their new electro-conductivity and thermal properties.[15] As to their biomedical applications, the most interesting property has been their high superficial area and the possibility of functionalizing it.[16] Because of its hydrophobic nature, graphene is not stable in aqueous solutions, complicating its use in biomedical applications.[17] The hydrophobicity problem was overcome in 2008 when the oxidized form of the graphene, the GO, was synthesized.[17] Many GO bioapplications include its intravenous administration. In these cases the red blood cells (RBC) are one of the main interactive structures, and thus hemocompatibility evaluation is crucial for suitable biomedical applications involving intravenous injections. Biocompatibility studies of GO began only recently.[18−20]

Model membranes are often used for the preliminary understanding of ligand−cell interaction. Frost et al.[21] observed for the first time that lipid membranes can bind GO. They proved that in a low-salt buffer the positively charged POPC:POEPC (3:1) membranes can bind GO, leading to the disruption of liposomes preadsorbed on GO sheets. No GO binding to negatively charged POPC:POPS (3:1) membranes could be observed.[21] Ip et al. described that in a physiological buffer GO can interact with positively charged DOTAP and neutral DOPC membranes. In addition they confirmed that, contrary to graphene, GO and rGO (both with hydrophobic and hydrophilic regions) can bind some DOPC vesicles without disruption. Again, they did not detect interaction between GO and negatively charged DOPG membranes.[22] In 2015 Liu and Chen were able to quantify the interaction between GO and lipid bilayers. They concluded that electrically neutral DOPC bilayers exhibited a greater interactive affinity with GO particles than positively charged (DOPC:DOEPC) ones.[23] They suggested that the interactions were dependent on buffer salinity and related the inability of achieving a 100% binding to the existence of repulsive hydration forces that can be operative when a well-hydrated particle approaches a lipid surface. Liu and Chen[23] tried to revert binding by changing the buffers in which aggregates were suspended, but they did not

Received: May 8, 2017
Revised: July 24, 2017
Published: August 3, 2017

DOI: 10.1021/acs.langmuir.7b01552
Langmuir 2017, 33, 8181−8191

achieve any dissociation. They also carried out leakage experiments, concluding that the interactions have as a result the formation of some membrane pores that would spontaneously repair.[23] Wu et al. demonstrated that at least four different types of interactions coexist between GO and lipid membranes: electrostatic repulsion and attraction, hydrogen bonding, and hydrophobic interactions.[24] Nevertheless, the relative importance of each one is unclear.

Until now, all studies have underlined the lack of interaction between GO and negatively charged model membranes, but these experiments do not match with the interactions observed between GO and Gram-negative bacteria[25] or erythrocytes,[18] both of which contain external negative charges. Liao et al. showed that nanometric GO (350 nm) induces a clear hemolytic effect (70% hemolysis) in comparison with 3 μm graphene sheets (10% hemolysis) after 3 h incubation.[18] Disruption of the erythrocyte membrane was related to electrostatic interactions between GO and the positive groups of phosphatidylcholine present in the outer monolayer of RBC membranes.[18] GO surface coatings may improve GO hemocompatibility. For example, chitosan coating by electrostatic adsorption[18] and bovine serum albumin or heparin coatings[26] almost suppressed the hemolytic activity of GO. It seems that biopolymer coatings could be useful to form a protective layer around the GO, reducing GO−RBC interaction and thus GO toxicity.[18,26] In this study we demonstrate the binding of GO to differently charged lipid membranes (including negative ones), and we use this knowledge to prepare lipid-coated GO in order to improve their hemocompatibility.

■ MATERIALS AND METHODS

Materials. GO was contributed by Graphenea (San Sebastian, Spain), and egg phosphatidylcholine (egg PC), bovine liver phosphatidylinositol (PI), phospatidylglycerol (PG), cholesterol (Chol), and sphingosine (Sph) were purchased from Lipid Products (South Nutfield, U.K.). Merocyanine was supplied by Sigma (St. Louis, MO). The fluorescent probe ANTS and its quencher DPX were purchased from Molecular Probes (Eugene, OR, U.S.A.). Sephadex G-25 M columns were obtained from GE Healthcare (Little Chalfont, Buckinghamshire, U.K.). Human blood was obtained from healthy informed donors. Pure human hemoglobin was supplied by Sigma-Aldrich (St. Louis, Missouri, U.S.A.). All other materials (salts and organic solvents) were of analytical grade.

Liposome Preparation. Lipids were mixed in chloroform:methanol (2:1), and the solvent was evaporated to dryness under a stream of N_2. Then the sample was kept under vacuum for 2 h to remove solvent traces, and the lipids were swollen in the appropriate buffer, usually 25 mM Hepes, 150 mM NaCl, pH 7.4. Small unilamellar vesicles (SUV) were obtained by sonicating the swollen lipid suspensions with a probe-type Soniprep 150 sonicator (MSK, London, U.K.). Large unilamellar vesicles (LUV) were also prepared from the swollen lipids, subjected to 10 freeze/thaw cycles before extrusion using the pertinent pore size Nuclepore filters (100 or 200 nm).[27] Vesicle size was checked by quasi-elastic light scattering using a Malvern Zeta-Sizer 4 spectrometer (Malvern Instruments, Worcestershire, U.K.). The SUV and LUV had average diameters of ∼40 and ∼100 or 200 nm, respectively. The lipid concentration was determined by phosphate analysis.

Quantification of GO Binding to Membranes. Mixtures of different GO/vesicle ratios as well as pure vesicle samples (as negative controls) were prepared in the pertinent buffer. In most cases GO and vesicles were mixed at the same *w*/*w* ratio and the same concentrations, 1 mg/mL each. All samples were centrifuged at 14,100*g* for 10 min; under these conditions GO and GO-bound vesicles, but not vesicles in suspension, precipitate. Once centrifuged, supernatants of all samples were collected, and the lipid concentration was determined by phosphate analysis, so that GO binding to vesicles could be indirectly calculated as "total lipid" minus "lipid in supernatant". The results are expressed as percent bound vesicle lipid. To achieve GO-bound vesicle dissociation, pellets containing GO−vesicle aggregates were resuspended in buffers of different salinity or pH,and then samples were centrifuged at 14,100*g* for 10 min. Once centrifuged, in order to quantify dissociated vesicles, supernatants were collected, and their lipid concentration was determined by phosphate analysis.

Confocal Microscopy Visualization of GO−Vesicle Aggregates. Direct visualization of SUV and LUV containing 1% Rhodamine-PE and mixtures of vesicles with GO in high-salt (25 mM Hepes, 150 mM NaCl, pH 7.4) and low-salt (25 mM Hepes, 0 mM NaCl, pH 7.4) buffers was achieved using an inverted confocal fluorescence microscope (Nikon D-ECLIPSE C1; Nikon, Melville, NY, U.S.A.). The excitation wavelength for Rhodamine-PE was 561 nm. The images were collected using band-pass filters of 593 ± 20 nm. All experiments were performed at room temperature. Image treatment was performed using the software EZ-C1 3.20 (Nikon).

Cryo-Electron Microscopy of GO Vesicle Aggregates. For cryo-EM analysis of liposomes (PC:PI or PC) incubated with GO, a 5 μL volume of 10 nm gold fiducial markers (Aurion BSA gold tracer 10 nm) was mixed with a 10 μL volume of the sample before vitrification process. The sample mixed with gold-markers was applied to a 200 mesh R3.5/1 holey carbon copper grid (Quantifoil Micro Tools GmbH, Jena, Germany) and frozen-hydrated following standard methods for cryo-EM, using a Vitrobot Mark III (FEI). For the tomographic tilt series acquisition, vitrified grids were cryo-transferred at liquid-nitrogen temperature into a 914 high tilt tomography cryo-holder (Gatan Inc., Warrendale, PA, U.S.A.). Vitrified grids were viewed at liquid-nitrogen temperature on a JEM-2000FS/CR field emission gun transmission electron microscope (Jeol Europe, Croissy-sur-Seine, France) operated at 200 kV. Different single-axis tilt series were collected under low-dose conditions on a UltraScan 4000, 4Kx4K CCD camera (Gatan Inc., Pleasanton, CA, USA), over a tilt range of ±64° with 1.5° increments and at underfocus values ranging from 6 to 8 μm, using the semiautomatic data acquisition software SerialEM.[28] Tilt-series were collected at a nominal magnification of 30 000× and a binning factor of 2 (2048 × 2048 pixels micrographs), thus producing a pixel size of 0.764 nm. The in-column omega energy filter helped to record images with improved signal-to-noise ratio by zero-loss filtering with an energy window of 60 eV centered at the zero-loss peak. CCD images in each tilt series were acquired at the same underfocus value and under the same low-dose conditions. The maximum total dose used for a tilt series was 90 electrons/$Å^2$ consisting of about 1−2 electrons/$Å^2$ for each digital image.

Tilt series were aligned using gold fiducial markers, and tomograms were reconstructed with IMOD software.[29] Tomograms were visualized with 3dmod and Chimera software

Atomic Force Microscopy (AFM). For a better understanding of the vesicle−GO sheet interaction, samples were scanned by AFM. Supported planar bilayers were prepared on high V-2 quality scratch-free mica substrates (Asheville-Schoonmaker Mica Co., Newport News, VA, U.S.A.). A total of 180 μL of assay buffer containing 3 mM $CaCl_2$ was added onto a 1.2 cm^2 freshly cleaved mica substrate mounted onto a BioCell (JPK Instruments, Berlin, Germany). Then 80 μL of sonicated 0.4 mM PC SUV was then added on top of the mica. BioCell temperature was gradually increased (5 °C steps every 5 min) up to 80 °C. Vesicles were left to adsorb and extend for 30 min keeping the sample temperature at 80 °C. Further 30 min were left to equilibrate samples at room temperature before performing five washes with non-$CaCl_2$ buffer in order to discard nonadsorbed vesicles and remove the remaining Ca^{2+} cations. (a) For pure GO visualization 200 μL of 0.5 mg/mL GO suspended in 150 mM NaCl, pH 7.4 was added onto the SPBs. After 20 min GO was attached to SPBs and three soft washes were performed with 150 mM NaCl, pH 7.4 in order to remove unattached GO sheets. (b) For mixtures, 2 μL of the GO−vesicle mixture at 1/1 ratio (*w*/*w*) were added onto the SPBs. As in the

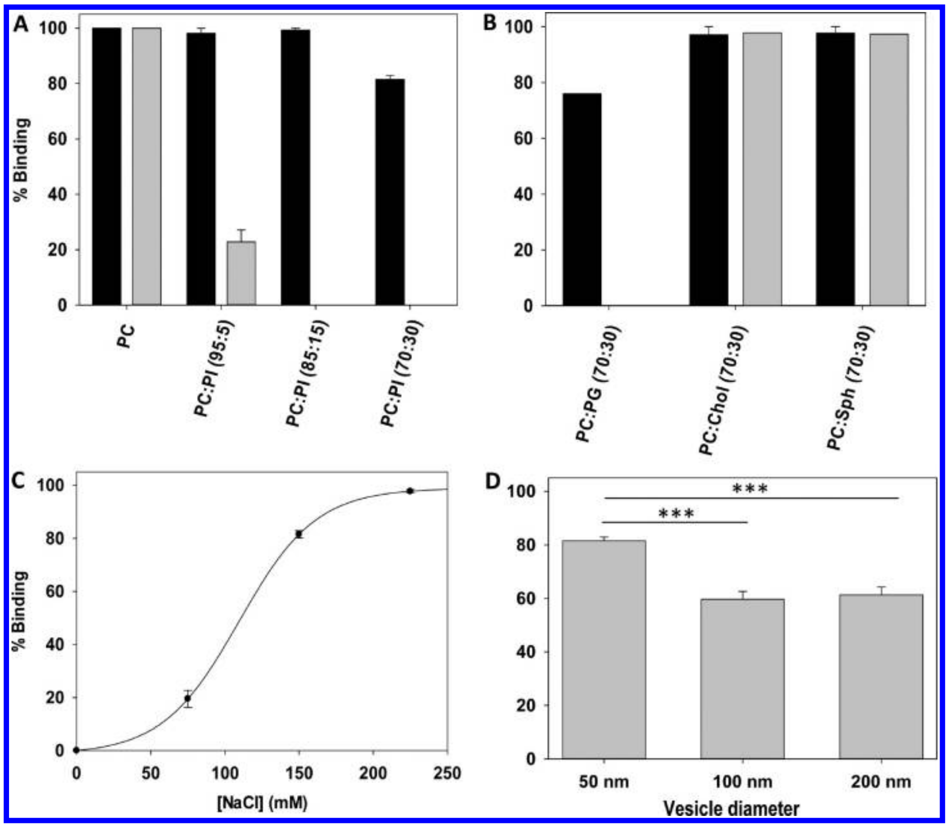

Figure 1. (A) Effect of PI on the binding of PC SUV to GO in high- and low-salt buffer. (B) Effect of the lipid membrane electric charge on the SUV-GO binding in high- and low-salt buffer. Black: high-salt; gray: low-salt. (C) Effect of [NaCl] on GO binding to PC:PI (70:30) SUV. (D) Effect of vesicle diameter on GO binding to PC:PI (70:30) SUV. Significance (*** $p < 0.001$) was tested with the Student's t test. All values represent average ± SD ($n = 3$).

previous case, 20 min were left and three soft washes with 150 mM NaCl, pH 7.4 were performed before sample visualization.

Topography analysis was performed under contact mode AFM scanning (constant vertical deflection) in a NanoWizard II AFM (JPK Instruments, Berlin, Germany). For proper measurements, the AFM was coupled to a Leica microscope and mounted onto a Halcyonics Micro 40 antivibration table (Halcyonics, Inc., Menlo Park, CA, U.S.A.) and inside an acoustic enclosure (JPK Instruments). V-shaped MLCT Si_3N_4 cantilevers (Bruker, Billerica, MA, U.S.A.) with nominal spring constants of 0.1 or 0.5 N/m were used for imaging. The sample thickness was estimated by cross-section height analysis.

Leakage Assay. In order to quantify vesicle disruption caused by GO, a leakage assay was performed as described by Ellens et al.[30] For this purpose, fluorescent 1-aminonaphtalene-3,6,8-trisulfonic (ANTS) and its quencher *N,N′-p*-xylylene-bis-pyridinium (DPX) were coencapsulated in SUV or LUV (20 mM ANTS, 70 mM DPX, 25 mM Hepes, 45 mM NaCl, pH 7.4), so that DPX would quench most of the ANTS fluorescence. A Sephadex G-25 chromatography column was used to separate liposomes from nonencapsulated probes, with an equi-osmolar buffer (25 mM Hepes, 150 mM NaCl, pH 7.4) used as the eluent. The leakage assay was performed at room temperature under continuous stirring in an SLM-AMINCO 8100 spectrometer with ANTS excitation and emission wavelengths of 355 and 520 nm, respectively, a 4 nm slit aperture, and a 460 nm filter. The basal signals obtained from pure vesicles (SUV or LUV) were considered as 0% leakage. For leakage data two different GO−vesicle mixture ratios were measured: 1 and 2.5 vesicle/GO (*w/w*). Samples were centrifuged at 14,100*g* for 10 min to discard GO (to avoid its absorption and dispersion properties), and the supernatant signal was measured. To obtain the 100% leakage signal, vesicles and GO aggregates in the precipitate were resuspended with supernatant, Triton X-100 was added, samples were centrifuged again under the same conditions, and supernatants were measured for fluorescence.

Blood Management and RBC Isolation. Human blood was collected from healthy donors and stored in EDTA tubes (BD Vacutainer Systems, Franklin Lakes, NJ, U.S.A.). Red blood cells were isolated by sequential centrifugations: 4 mL of whole blood was added to 50 mL of 150 mM NaCl buffer and centrifuged at 3000*g* for 10 min to isolate RBC from serum. This purification step was repeated five times, and finally the washed RBC were diluted to 10^9 cell/ml in 25 mM Hepes, 150 mM NaCl, pH 7.4 buffer.

Hemolytic Activity. To test the hemolytic activity of GO, serial dilutions of GO starting from 2 mg/mL and a constant RBC concentration (5×10^8 RBC/ml) in a total volume of 200 μL were prepared in 25 mM Hepes, 150 mM NaCl, pH 7.4 buffer. Then samples were centrifuged at 14,100*g* for 10 min, and supernatants that contained leaked hemoglobin were collected. Supernatants were diluted 10 times in distilled H_2O before measuring absorption at 412 nm with a UV mini 1240 spectrophotometer (Shimadzu, Kyoto, Japan). Intact RBC and Triton X-100 lysed RBC samples were used as negative and positive controls, respectively.

For measuring GO−SUV aggregate-induced hemolysis, GO was premixed with PC or PC:PI SUV at a 2.5/1 ratio (*w/w*), and hemolysis was measured as in the previous case.

Estimation of Hemolysis. Hemolysis was estimated using the equation

$$\text{hemolysis}(\%) = \frac{\text{EG} - \text{NC}}{\text{PC} - \text{NC}} \times 100\%$$

where EG, NC, and PC are experimental group, negative control, and positive control, respectively.

Hemoglobin and GO Binding. As hemoglobin is positively charged at physiological pH,[31] it can interact with negatively charged GO sheets. Taking into account that GO is discarded before hemolytic measurements, part of the RBC-leaked hemoglobin will join GO and

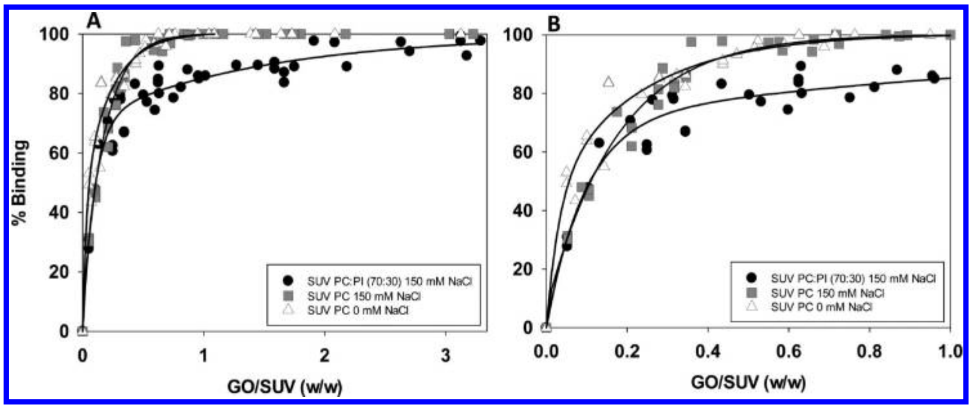

Figure 2. GO binding to PC or PC:PI (70:30) SUV at different GO/SUV ratios (*n* = 3). Panel B shows an expanded area of panel A.

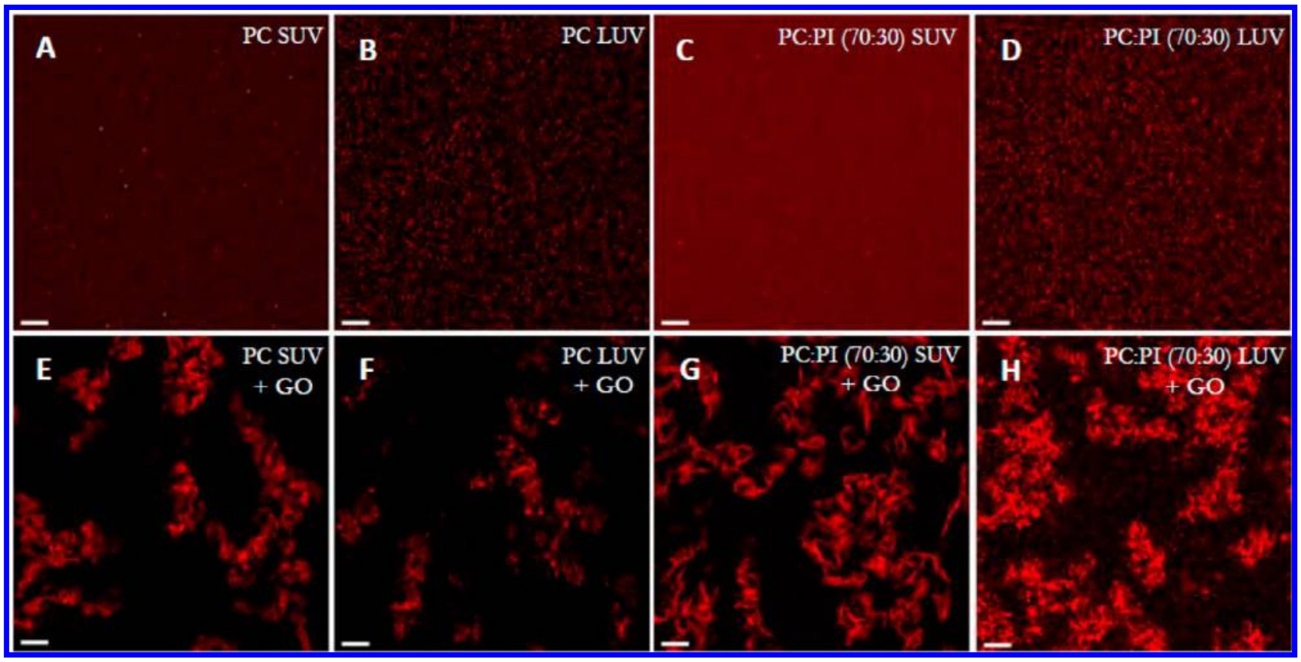

Figure 3. Confocal microscopy images. (A) PC SUV. (B) PC LUV. (C) PC:PI (70:30) SUV. (D) PC:PI (70:30) LUV. (E) PC SUV + GO. (F) PC LUV + GO. (G) PC:PI (70:30) SUV + GO. (H) PC:PI (70:30) LUV + GO. All in 150 mM NaCl. All mixtures at vesicle/GO (*w*/*w*) ratio 1. Bar: 5 μm.

will also be lost. This coexisting binding should be quantified for a correct estimation of GO-induced hemolysis.

Two types of measurements were performed: On one hand, sonicated RBC-leaked hemoglobin and GO binding and, on the other hand, commercially available pure hemoglobin and GO binding. GO–hemoglobin binding was calculated using the same technique described for hemolysis measurements, but in this case the supernatant signal would correspond to nonbound hemoglobin.

■ RESULTS

Effect of Electric Charge and Ionic Strength on Model Membrane Binding to GO. GO (1 mg/mL) and SUV (1 mg/mL) were mixed to perform this experiment. As seen in Figure 1A, neutral PC vesicles bind GO in both high- and low-salt buffers. Furthermore, the presence of negatively charged PI in PC-based membranes decreases binding between liposomes and GO. To verify that these differences were exclusively due to the membrane charge and not to morphological reasons, mixtures of PC with negatively charged PG, neutral Chol, or positively charged Sph were also studied. As seen in Figure 1B, PC:PG (70:30) SUV showed 76 ± 3.1% binding to GO in 150 mM NaCl and 0% in 0 mM NaCl buffer. Essentially similar results were obtained when the negatively charged lipid was PI instead of PG. PC:PI (70:30)-GO binding data were 81 ± 2.1% and 0%, respectively (Figure 1A). PC:Chol (70:30) SUV (electrically neutral), as well as positively charged PC:Sph (70:30) SUV, showed 100% binding in both high- and low-salt buffers (Figure 1B). These results indicate that ionic strength has a great influence on the GO binding of negatively charged membranes.

Taking into account the importance of salt concentration, the NaCl effect on PC:PI (70:30) SUV binding to GO was studied in more detail. Figure 1C shows that the [NaCl] increase is related to enhanced binding, achieving a value of 100% above 225 mM NaCl.

Effect of Vesicle Diameter on Vesicle Binding to GO. Figure 1D shows that vesicle size has a marked influence on the amount of binding. Comparing 100 and 200 nm diameter PC:PI (70:30) LUV with 50 nm SUV, the former allowed considerably less binding. Student's *t* test showed a statistically significant difference between 100 or 200 nm LUV and 50 nm

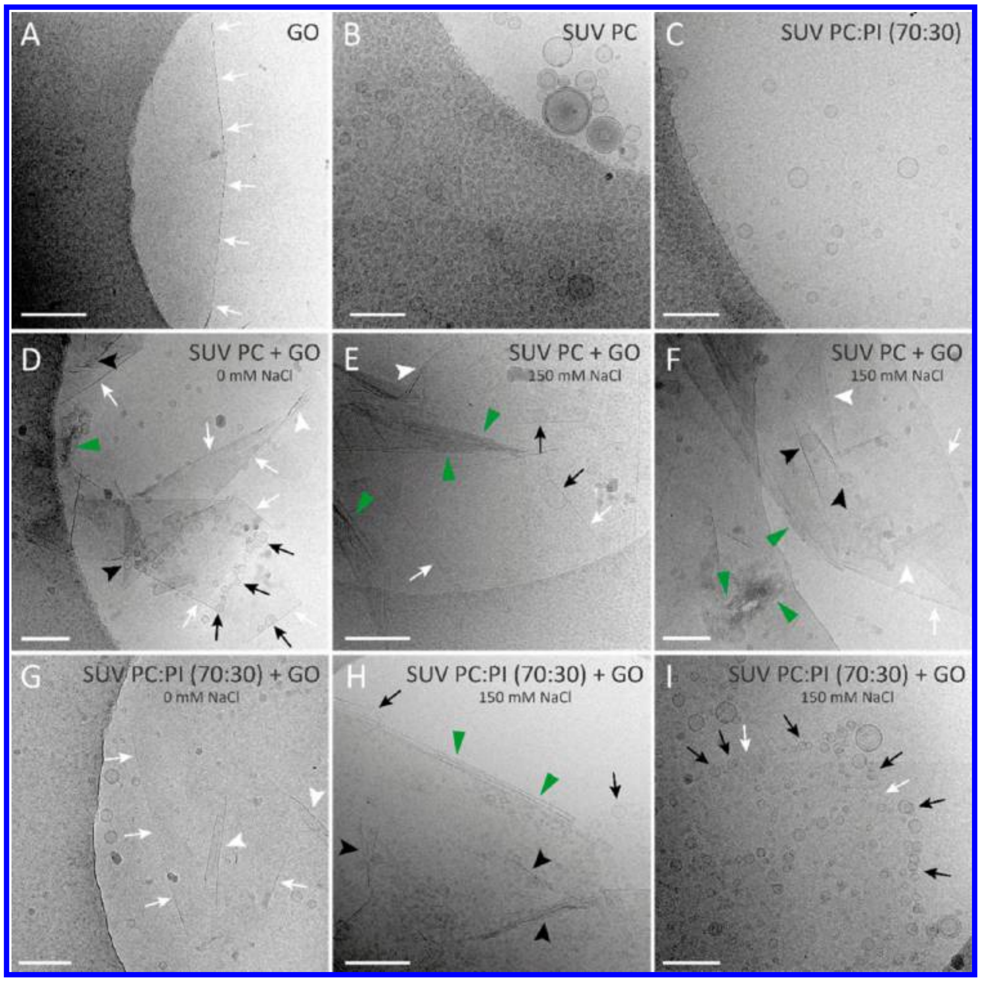

Figure 4. Cryo-TEM imaging of GO and SUV. (A) GO sheets. The sheet edges are shown by white arrows. (B) PC SUV. (C) PC:PI (70:30) SUV. (D) GO-PC SUV mixture in 0 mM NaCl. (E and F) GO-PC SUV mixture in 150 mM NaCl. (G) GO-PC:PI SUV mixture in 0 mM NaCl. The sheet edges are marked with white arrows. (H and I) GO-PC:PI SUV mixture in 150 mM NaCl. Along the panels: GO sheet edges are marked with white arrows; interactions between SUV and planar GO surfaces are labeled with black arrows; white arrowheads indicate folded GO surfaces; black arrowheads point to curved GO surfaces in contact with SUV; stacked GO structures are marked with green triangles. Bar 100 nm.

SUV binding to GO. No significant difference was observed between 100 and 200 nm LUV binding to GO. Vesicle size effect on GO binding could be related to accessibility parameters. The relatively larger 100 and 200 nm LUV vesicles would bump into more repulsive GO groups while interacting with the sheets. On the contrary 50 nm SUV would have an easier access to interactive hydrophobic GO regions.

GO Binding Capacity. Having shown that lipid membranes can interact with GO sheets, their binding properties were quantitatively explored for various SUV lipid compositions (Figure 2). Some differences were observed, particularly for the GO/SUV *w/w* ratio producing 50% binding that was about 0.05 for PC SUV in the absence of 150 mM NaCl and of about 0.1 for PC and for PC:PI SUV in the presence of 150 mM NaCl (Figure 2 B). Moreover PI-containing vesicles required about 5-fold GO concentrations to achieve 100% SUV binding levels (Figure 2 A). Because of their negatively charged groups, PC:PI vesicles are always more exposed to the repulsion forces exerted by negatively charged GO groups, and thus vesicles of this composition will need larger amounts of GO to find an equivalent amount of noncharged area that will permit binding.

Confocal Fluorescence Microscopy. Mixtures of SUV or LUV and GO were visualized by confocal fluorescence microscopy in order to explore the possibility of aggregate formation. As SUV size (50 nm) is below the resolution limit of the confocal microscope (~200 nm), SUV control images (Figure 3A,C) appear as a red homogeneous background. However, LUVs (~200 nm) can be distinguished as little red dots (Figure 3B,D). When GO is added to phospholipid vesicles, the red fluorophore appears to concentrate in some specific regions, in the form of aggregates 5−25 μm in size, indicating that GO particles are acting as nucleation centers for vesicles and that the lipid-coated particles are forming larger aggregates (Figure 3E−H). No differences between PC or PC:PI (70:30) vesicles in GO aggregate formation can be appreciated, perhaps due to the resolution limit of the confocal microscope.

Cryo-EM. Vesicle−GO cryo-EM images demonstrate the presence of PC SUV-GO aggregates in high- and low-salt buffers (Figure 4D−F). As shown in Figure 4E,F, in high-salt buffer mixtures, some vesicles appear squashed when attached to GO. It also seems that salt induces GO sheet stacking (Figure 4E,F). The considerable decrease of observable intact vesicles comparing PC SUV in the absence (Figure 4 B) and presence of GO (Figure 4D−F) can indicate that a large amount of vesicles are disrupted and spread over the GO sheets upon interaction. When PC SUV vesicles are mixed with GO in

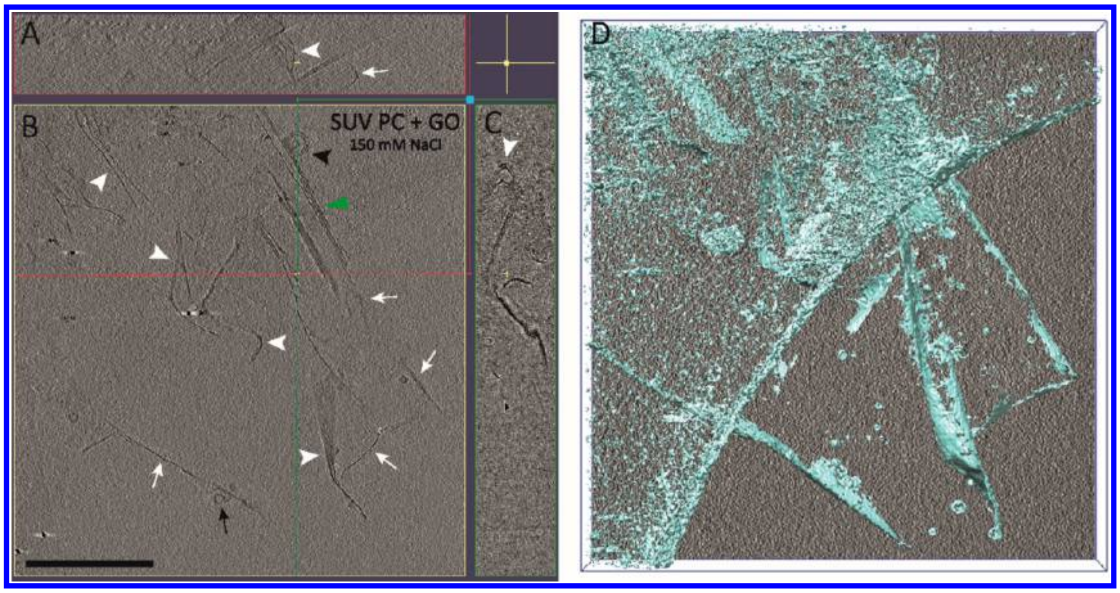

Figure 5. 3D reconstruction of GO sheets incubated with PC SUV at 150 mM of NaCl concentration by cryo-EM. This figure shows different representations of the same 3D tomogram reconstructed from tilt-series images collected in the same area of interest at 30 000× magnification (5 μm under focus). (A) An orthogonal view (XZ) of the 3D reconstruction taken through the 3D reconstruction along the red line marked in panel B. (B) Tomographic central XY section of the reconstructed tomogram showing the interaction between GO surface and SUV. Black arrowheads indicate the folding of the GO surface in contact with SUV, white arrowheads indicate folded GO surfaces, and stacked GO structures are marked with green triangles. Black arrows indicate the edges of planar GO surfaces in contact with SUV, and white arrows indicate the areas of the GO surface without the presence of SUV. Scale bar, 100 nm. (C) An orthogonal view (YZ) of the 3D reconstruction taken through the tomogram along the green line marked in panel B. (D) Electron density map representation of the tomogram viewed together in surface and solid styles with Chimera software. A video of this tomogram viewed from different perspectives (as consecutive slices in XY, XZ, and YZ plane orientation and as an electron density map) can be found in the Supporting Information.

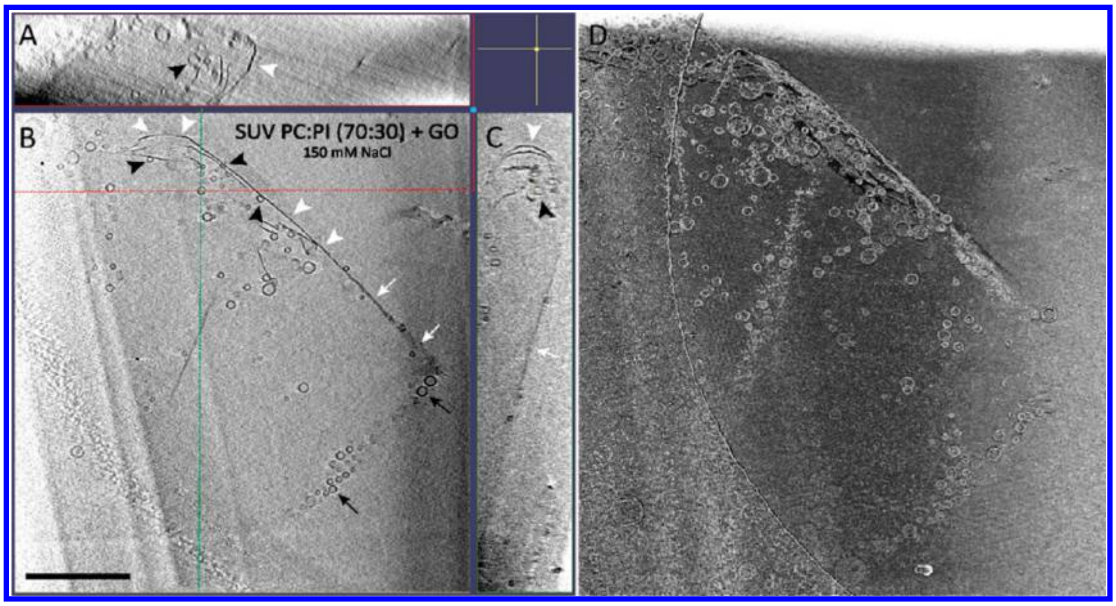

Figure 6. 3D reconstruction of GO sheets incubated with PC:PI (70:30) SUV at 150 mM of NaCl concentration by cryo-ET. This figure shows different representations of the same 3D tomogram reconstructed from tilt-series images collected in the same area of interest at 30 000× magnification (5 μm under focus). (A) An orthogonal view (XZ) of the 3D reconstruction taken through the 3D reconstruction along the red line marked in panel B. (B) Tomographic central XY section of the reconstructed tomogram showing the interaction between GO surface and SUV. Black arrowheads indicate the folding of GO surface in contact with SUV. Black arrows indicate the edges of planar GO surfaces in contact with SUV, and white arrows indicate the areas of GO surface without the presence of SUV. Scale bar, 100 nm. (C) An orthogonal view (YZ) of the 3D reconstruction taken through the tomogram along the green line marked in panel B. (D) Electron density map representation of the tomogram viewed together in surface and solid styles with Chimera software. A video of this tomogram viewed from different perspectives (as consecutive slices in XY, XZ, and YZ plane orientation and as an electron density map) can be found in the Supporting Information.

a low-salt buffer, the total amount of bound vesicles appears to be larger (Figure 4D).

In PC:PI SUV-GO mixtures, intact bound as well as nonbound vesicles can be seen in high-salt mixtures (Figure

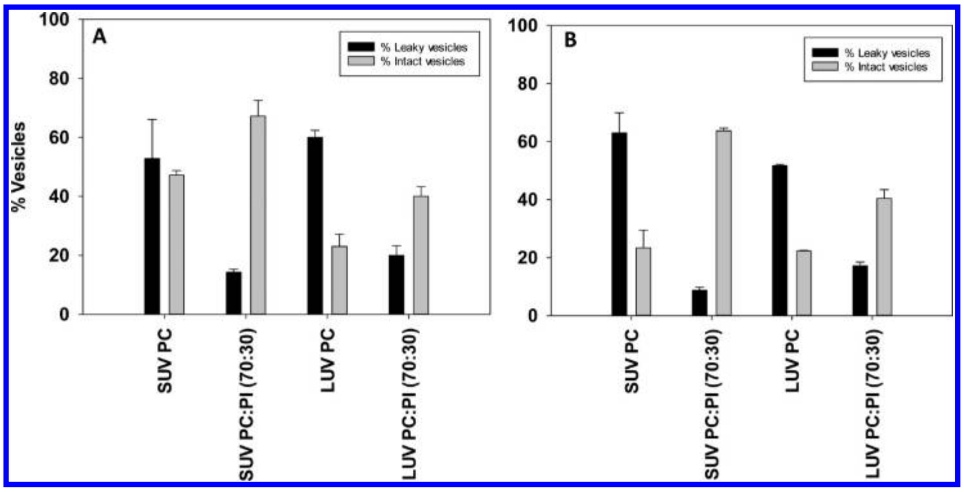

Figure 7. Vesicle leakage assay. Percent leaky and intact vesicles when the vesicle/GO (*w*/*w*) ratio is (A) 1 or (B) 2.5. All values represent average ± SD (*n* = 3).

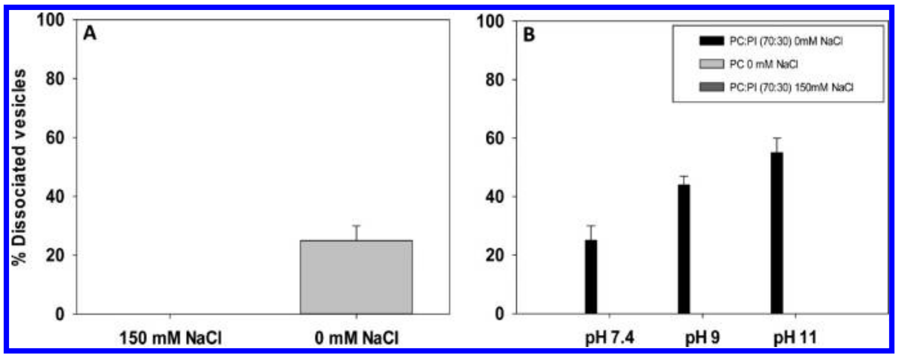

Figure 8. Vesicle dissociation from GO–SUV aggregates. (A) Dissociated PC:PI SUV from SUV–GO aggregates in high- and low-salt buffers. (B) Salinity and pH effects on vesicle dissociation (pH over 11 could not be operated because of stability reasons of the phospholipid ester bonds). All values represent average ± SD (*n* = 3).

4H,I), in agreement with data from quantification experiments (Figure 1A). In Figure 4I intact vesicles appear following a well-marked border, indicating that these vesicles are bound around a GO sheet. However, in low-salt buffer images, GO sheets and PC:PI vesicles do not appear to contact (Figure 4G).

GO sheets incubated with SUV at 150 mM NaCl were studied by cryo-EM tomography. A 3D-reconstruction can be seen in Figures 5 and 6, respectively, for electrically neutral (PC) and negatively charged (PC:PI) vesicles. Each of these figures show different representations of a given 3D tomogram reconstructed from tilt-series images collected from an area of interest. The corresponding videos can be found in the Supporting Information. In the tomographic central XY section of the 3D reconstruction of GO sheets incubated with PC SUV at 150 mM NaCl (Figure 5B), few intact vesicles attached to GO can be distinguished. Confirming the observations in Figure 4 for the system in 150 nM NaCl, it can also be seen that GO sheets are arranged in stacks. The orthogonal views XZ and YZ and the electron density map representation (Figure 5A,C,D) provide further details of the interaction: folded GO sheets, sometimes in contact with SUV, edges of planar GO surfaces in contact with SUV, and areas of GO sheets devoid of vesicles can be found.

In the mixture of GO and PC:PI SUV in the presence of salt (Figure 6), the main observation in the tomographic central XY section (Figure 6B) is the considerable amount of intact vesicles attached to GO, both to folded sheets and to edges of planar GO surfaces. Again the orthogonal views XZ and YZ and the electron density map (Figure 6A,C,D) provide a thorough view of the occurring interaction. Tomography provides structural detail to the chemical measurements of Figures 1 and 2 and allows a 3D representation of the conventional microscopic observations in Figures 3 and 4.

Leakage Assay. In order to quantify GO-sheet-induced vesicle disruption and the dependence of vesicle charge and size (SUV or LUV), leakage experiments were performed at vesicle/GO ratios (*w*/*w*) of 1.0 (Figure 7A) and 2.5 (Figure 7B). In all cases, but particularly with PC SUV, the presence of GO sheets caused release of vesicle aqueous contents. The proportion of intact vesicles was estimated from the amount of fluorescent probe released after addition of the detergent Triton X-100. No statistical difference was observed between the two vesicle/GO ratios nor between the two vesicle sizes. Nevertheless, differences were present between differently charged vesicles: while leakage is predominant with pure PC vesicles, PC:PI (70:30) vesicles remain mostly intact.

Dissociation of GO–Vesicle Aggregates. In order to test whether GO–vesicle binding was or was not reversible, SUV–GO aggregates were transferred to a fresh medium. When PC:PI (70:30) SUV–GO aggregates were resuspended in a low-salt buffer, 20% of the bound vesicles were dissociated. However, when resuspension was performed with a high-salt buffer, no dissociation could be achieved (Figure 8A).

DOI: 10.1021/acs.langmuir.7b01552
Langmuir 2017, 33, 8181–8191

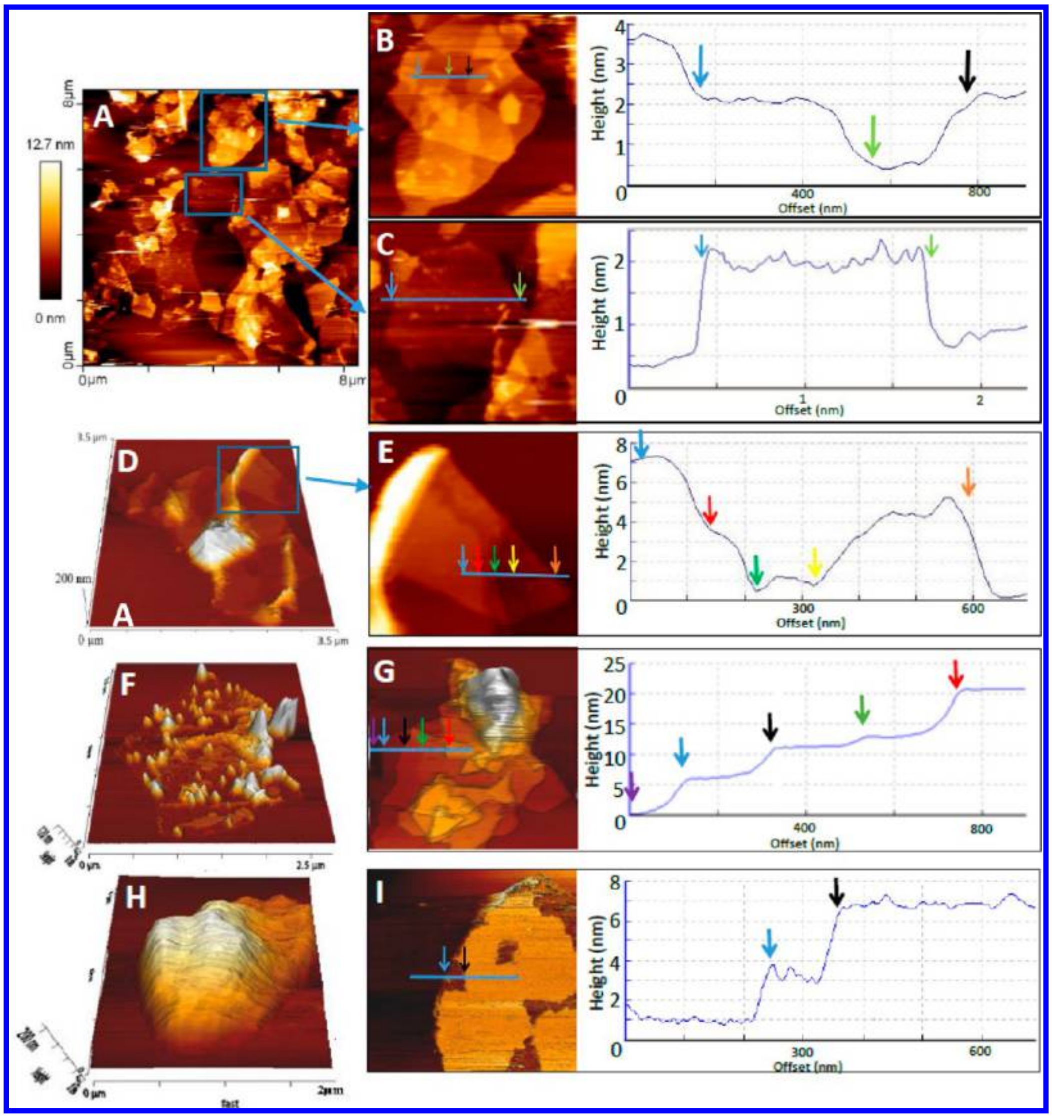

Figure 9. AFM images. (A) Stacked GO sheets in 150 mM NaCl buffer. (B) Zoom of Figure 7A where 1.5 nm thick stacked GO sheets are seen (three stacked GO sheets are marked with blue, green, and black arrows). (C) Zoom from Figure 7A where a 1.5 nm thick single GO sheet is seen. (D) 3D reconstruction of PC LUV-GO mixture. (E) Zoom of Figure 7D, where a bilayer (blue arrow) spreads over two GO sheets (between red and yellow arrows). The orange arrow marks a bilayer at the edge of the GO sheet. (F) 3D reconstruction of the PC:PI (70:30) LUV−GO mixture, where extended and semiextended vesicles are seen. (G) PC:PI (70:30) LUV−GO mixture. Arrows: Purple, GO sheet; blue, GO sheet + bilayer; black, + bilayer; green, + GO sheet; red, + GO sheet + bilayer. (H) 3D reconstruction of the PC:PI (70:30) LUV−GO mixture where three or four intact LUV are bound to a GO sheet. (I) LUV extension over a GO sheet and corresponding topographic profile.

Dissociation could be enhanced when a salinity change was combined with a pH change. High pH increases electrostatic repulsions between vesicles and GO due to negative charge enhancement. As seen in Figure 8B, a maximum of 60% vesicle dissociation could be achieved when aggregates were resuspended in a low-salt pH 11 buffer. Dissociation of pure PC SUV−GO aggregates could not be achieved under any conditions.

AFM. AFM topographic studies provide yet further insight into our understanding of GO−vesicle interactions. In particular intact and extended vesicles, the latter having presumably released their aqueous contents, can be distinguished. As seen in Figure 9A−C, under high-salt conditions, 1.5−2 nm thick GO sheets tend to stack. When GO sheets are mixed with pure PC LUV (200 nm), intact vesicles are seen, mainly bound to GO sheet borders (Figure 9 D). Moreover, 4−5 nm thickness bilayers are seen on top of GO sheets (Figure 9E).

Using a mixture of 200 nm PC:PI (70:30) LUV and GO, semiextended vesicles and 1.5−2 nm thickness GO sheets can be seen (Figure 9F,G). Figure 9H shows a 3D reconstruction of three or four intact PC:PI (70:30) LUV bound to a GO sheet. Figure 9I shows 4 nm thick PC:PI (70:30) LUV extensions over a 2 nm thick GO sheet.

Hemolysis and Hemolysis Protection. The phenomenon of GO-induced release of LUV aqueous contents can also be observed with erythrocytes in the form of hemolysis. As the GO concentration is increased, hemolysis is also enhanced reaching a maximum of about 80% with a 0.25 mg/mL GO concentration (Figure 10A). Taking into account the observed decrease in hemolysis above this GO concentration, it was suggested that GO−hemoglobin binding could be interfered in the hemolysis measurement, so GO−hemoglobin binding was

DOI: 10.1021/acs.langmuir.7b01552
Langmuir 2017, 33, 8181−8191

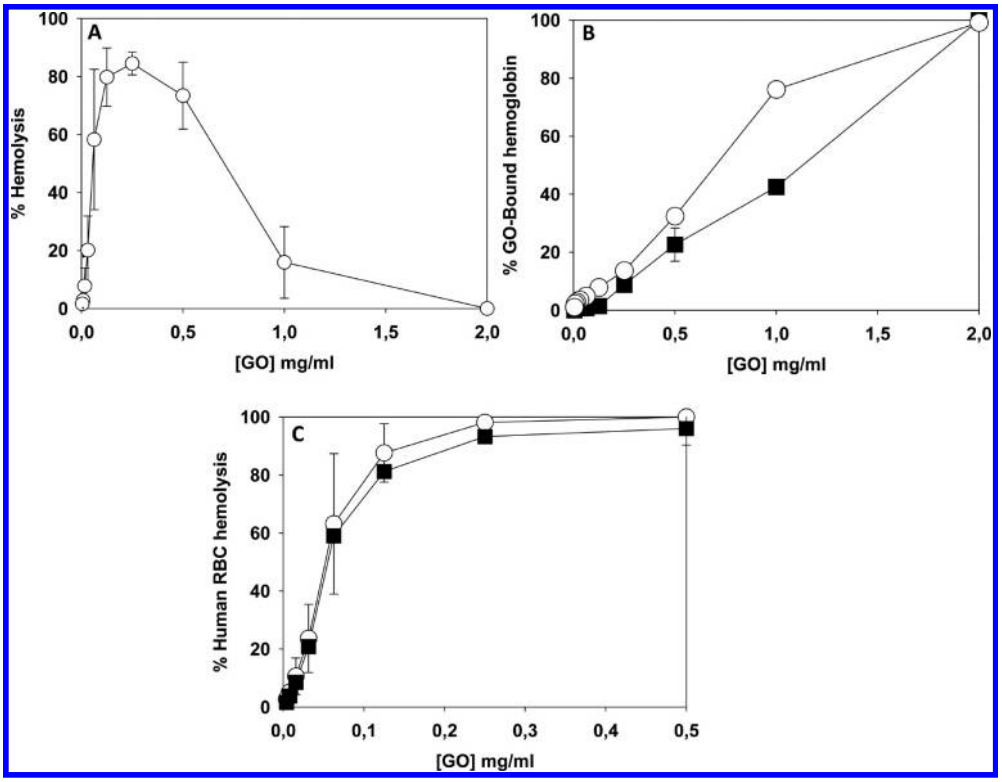

Figure 10. (A) Apparent GO-induced human RBC hemolysis in a 5 × 10^8 RBC/mL suspension as a function of GO concentration. All values represent average ± SD (n = 4). (B) GO−hemoglobin binding. Squares represent binding of sonicated RBC hemoglobin and GO as a function of GO concentration. White circles represent binding of commercial hemoglobin (equivalent to 5 × 10^8 RBC/mL) as a function of GO concentration. All values represent average ± SD (n = 4). The statistical differences ($^*p < 0.05$ and $^{***}p < 0.001$) have been estimated with a Student's t test. (C) Corrected GO-induced hemolysis. Black squares show the combination of GO and human RBC leaked hemoglobin binding and hemolysis signal (Figure 4A). Circles show the combination of GO and commercial hemoglobin binding with hemolysis signal (Figure 4A).

quantified. Figure 10B shows that GO and hemoglobin have a considerable affinity, reaching 100% binding at 2 mg/mL GO for 5 × 10^8 RBC. Comparing both hemoglobin sources, binding of commercial hemoglobin to GO is higher than binding of sonicated RBC-leaked hemoglobin at all measured concentrations, although the differences are significant only at 0.5 and 1.0 mg/mL GO (Figure 10B).

Because of this interaction, the hemolysis signal in Figure 10A will only be indicating non-GO bound hemoglobin. Therefore, as shown in Figure 10C, real hemolysis has to be recalculated by adding GO-bound hemoglobin (Figure 10B) and free hemoglobin (Figure 10A). Figure 10C shows that hemolysis increases with GO concentration reaching a 100% hemoglobin leakage above 0.5 mg/mL GO.

Figure 11 shows the decreased hemolysis that occurs when GO sheets are premixed with different SUV. When GO sheets are premixed with PC:PI (70:30) SUV, hemolysis is decreased by at least 60% in a 0.5 mg/mL GO suspension. When GO sheets are premixed with pure PC SUV, hemolysis is almost totally suppressed at a 0.5 mg/mL GO concentration.

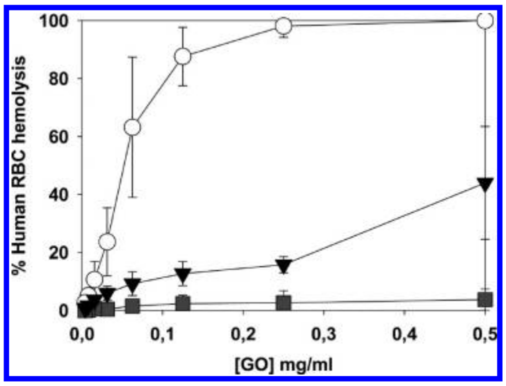

Figure 11. Hemolysis induced in RBC by GO or GO-LUV aggregates (5 × 10^8 RBC/mL). Circles: pure GO; triangles: GO-PC:PI SUV; squares: GO-PC SUV.

■ DISCUSSION

GO Binding to Lipid Vesicles. Electrically positive and neutral model membrane−GO interactions have been shown in several publications.[21−23] Nevertheless, previous studies have underlined the lack of interaction between GO and negatively charged model membranes.[21,22] In a low-salt medium, the most relevant cause of differences in the binding of GO to pure PC or PC:PI (70:30) SUV (Figure 1A) is probably the electrostatic repulsion that exists between PI and GO negative charges. As pure PC vesicles are electrostatically neutral, binding will be caused by nonelectrostatic interactions, e.g., hydrophobic interactions (although other interactions such as hydrogen bonding cannot be discarded). Nevertheless, in vesicles containing negatively charged PI, electrostatic repulsions will occur between the GO negative charges (carboxyl and hydroxyl groups) and PI, and thus binding will depend on the balance between repulsive and other types of forces (maybe hydrophobic).

The enhancement of PC:PI vesicle binding to GO that occurs when buffer salinity is increased may be similar to what occurs in the renaturation process of DNA. DNA, after being denatured, needs a high-salt concentration because Na^+ ions can stabilize negative charges of phosphate groups of each DNA strand. This high-salt concentration masks the charge repulsions that destabilized negatively charged phosphodiester strands and achieves renaturation of DNA strands.[32] Extending this phenomenon to our study, salinity will stabilize the repulsions that exist between GO carboxyl groups and PI phosphates. Thus, electrostatic interactions (attractive and repulsive) have a crucial importance, but as the existence of hydrophobic regions in GO has been proven (Figure 1 E), hydrophobic interactions between aromatic rings of GO and hydrophobic regions of lipids probably contribute to the binding.[24]

Vesicle Extension/Disruption on GO Surfaces. Frost et al. demonstrated that GO causes disruption of preadsorbed liposomes on GO sheets.[21] Moreover Ip et al. proposed that GO can bind some neutral vesicles without any disruption. In our case, as seen in the microscopy images and also shown by the leakage assay, pure PC vesicles will be disrupted when interacting with GO sheets (Figure 7), and disrupted membranes will extend and cover the GO sheets (Figure 9D,E). Even so, some nondisrupted vesicles will also bind GO sheets (Figures 4D−F and 5), probably creating electrostatic or H-bound interactions between lipid polar head groups and functionalized GO groups. However, PC:PI vesicles are mostly bound to GO without disruption/extension (Figures 4H,I and 6).

Vesicles do not exhibit a specific pattern when interacting with GO. AFM images (Figure 9) that show extended, semiextended, and intact vesicles lead to the idea that the heterogeneous molecular structure of GO sheets makes each vesicle follow a different morphological evolution depending on the region of GO that it first interacts with.

Vesicle Dissociation. Liu and Chen tried to revert binding by changing the buffers in which aggregates were suspended, but they did not achieve any dissociation.[23] In our studies, removal of Na^+ ions from PC:PI vesicle−GO aggregates induces the partial dissociation of bound vesicles (Figure 8A). Dissociation occurs because the stabilizing role of these ions disappears. In addition, when this salinity change is combined with a pH increase, PC:PI dissociation from GO is also enhanced (Figure 8B). This occurs because free OH^- present in the medium will increase the negative charges of GO and PI and as a consequence also their repulsion phenomena. As pure PC vesicles are electrostatically neutral, even if GO becomes more negative, repulsion forces will not be detectable.

Hemolysis and Antihemolytic Protection. Biocompatibility studies of GO began recently, and most of them have demonstrated that GO induces a severe cytotoxicity in many human cells such as erythrocytes[18,19] and skin fibroblasts.[18]

As GO concentration is increased, hemolysis also increases (Figure 10C). GO will first disrupt the RBC, and the resulting free membranes will bind to GO sheets. Below 0.25 mg/mL, GO sheets will probably be coated with RBC membranes, so hemoglobin cannot bind to GO and hemoglobin in solution can be easily measured. Over 0.25 mg/mL GO however, as noncoated GO sheets are present, hemolysis decreases due to the concurrent hemoglobin−GO binding (Figure 10A). In GO−hemoglobin binding controls (Figure 10B), binding between GO and RBC-leaked hemoglobin is lower than between GO and commercial hemoglobin. As RBC membranes are also present in the above-mentioned control, a lower signal probably occurs due to a competitive phenomenon between hemoglobin and RBC membranes for GO binding. Therefore, hemolysis must be recalculated by adding the hemoglobin−GO binding percentage to the initially calculated hemolysis signal. When this correction is performed, 0.5 mg/mL GO is enough to produce full hemolysis of 5×10^8 RBC/mL (Figure 10C).

GO−SUV mixtures appear to consist of lipid-coated GO sheets that notably reduce hemolysis (Figure 11). It has been demonstrated that chitosan coating by electrostatic adsorption[18] and bovine serum albumin or heparin coatings[26] almost suppressed the hemolytic activity of GO. In our lipid-coating case, the antihemolytic phenomenon is more noticeable when SUV are electrically neutral; that is, PC SUV have a greater tendency to disrupt and extend over GO sheets than PC:PI SUV (Figures 7 and 9), and the coated sheet area will be larger in the former case. Thus, with PC SUV a smaller number of GO hemolytic regions will be exposed, achieving almost complete inhibition of hemolysis (Figure 11). This would indicate that the toxicity of GO in blood may be largely overcome with a good coating of GO by liposomes.

■ ASSOCIATED CONTENT

Supporting Information

The Supporting Information is available free of charge on the ACS Publications website at DOI: 10.1021/acs.langmuir.7b01552.

Video 1: Cryo electron tomography showing the 3D reconstruction of GO sheets incubated with PC SUV. (MP4)

Video 2: Cryo electron tomography showing the 3D reconstruction of GO sheets incubated with PC:PI (70:30 mol ratio) SUV. (MP4)

■ AUTHOR INFORMATION

Corresponding Author

*E-mail: felix.goni@ehu.es.

ORCID

Félix M. Goñi: 0000-0001-6270-9216

Notes

The authors declare the following competing financial interest(s): B. A. and A. Z. are employees of Graphenea, San Sebastian, Spain. The remaining authors declare no competing financial interest.

■ ACKNOWLEDGMENTS

This work was supported in part by FEDER-MINECO Grant No. BFU 2015-66306-P and by Grant No. IT-849-13 from the Basque Government. B.G.-M. is a predoctoral student supported by the University of the Basque Country.

■ ABBREVIATIONS

AFM, atomic force microscopy
ANTS, 1-aminonaphtalene-3, 6, 8-trisulfonic
DPX, *N,N′-p*-xylylene-bis-pyridinium
Chol, cholesterol
DOEPC, 1,2-dioleoyl-*sn-glycero*-3-ethylphosphocholine
DOPC, 1,2-dioleoyl-*sn*-glycero-3-phosphocholine
DOPG, 1,2-dioleoyl-*sn*-glycero-3-phosphoglycerol
DOTAP, 1,2-dioleoyl-3-trimethylammonium-propane
GO, graphene oxide
LUV, large unilamellar vesicle/s

POEPC, 1-palmitoyl-2-oleyl-*sn*-glycero-3-ethylphosphocholine
POPC, 1-palmitoyl-2-oleoyl-*sn*-glycero-3-phosphocholine
POPS, 1-palmitoyl-2-oleoyl-*sn*-glycero-3-phospho-L-serine
PC, phosphatidylcholine
PI, phosphatidylinositol
PG, phospatidylglycerol
RBC, red blood cells
Sph, sphingosine
SUV, small unilamellar vesicle/s

■ REFERENCES

(1) Kuila, T.; Bose, S.; Khanra, P.; Mishra, A. K.; Kim, N. H.; Lee, J. H. Recent advances in graphene-based biosensors. *Biosens. Bioelectron.* **2011**, *26*, 4637−4648.

(2) Unnikrishnan, B.; Palanisamy, S.; Chen, S. M. A simple electrochemical approach to fabricate a glucose biosensor based on graphene-glucose oxidase biocomposite. *Biosens. Bioelectron.* **2013**, *39*, 70−85.

(3) Sun, W.; Zhang, N.; Li, A.; Zou, W.; Xu, W. Preparation and evaluation of N3-O-toluylfluorouracil-loaded liposomes. *Int. J. Pharm.* **2008**, *353*, 243−250.

(4) Lu, C. H.; Li, J.; Liu, J. J.; Yang, H. H.; Chen, X.; Chen, G. N. Increasing the sensitivity and single-base mismatch selectivity of the molecular beacon using graphene oxide as the ″nanoquencher″. *Chem. - Eur. J.* **2010**, *16*, 4889−4894.

(5) Ryoo, S. R.; Kim, Y. K.; Kim, M. H.; Min, D. H. Behaviors of NIH-3T3 fibroblasts on graphene/carbon nanotubes: proliferation, focal adhesion, and gene transfection studies. *ACS Nano* **2010**, *4*, 6587−6598.

(6) Nayak, T. R.; Andersen, H.; Makam, V. S.; Khaw, C.; Bae, S.; Xu, X.; Ee, P. L.; Ahn, J. H.; Hong, B. H.; Pastorin, G.; Özyilmaz, B. Graphene for controlled and accelerated osteogenic differentiation of human mesenchymal stem cells. *ACS Nano* **2011**, *5*, 4670−4678.

(7) Kim, S. H.; Lee, J. E.; Sharker, S. M.; Jeong, J. H.; In, I.; Park, S. Y. In Vitro and In Vivo Tumor Targeted Photothermal Cancer Therapy Using Functionalized Graphene Nanoparticles. *Biomacromolecules* **2015**, *16*, 3519−3529.

(8) Zhao, X.; Su, Y.; Liu, Y.; Li, Y.; Jiang, Z. Free-Standing Graphene Oxide-Palygorskite Nanohybrid Membrane for Oil/Water Separation. *ACS Appl. Mater. Interfaces* **2016**, *8*, 8247−8256.

(9) Sun, X.; Liu, Z.; Welsher, K.; Robinson, J. T.; Goodwin, A.; Zaric, S.; Dai, H. Nano-Graphene Oxide for Cellular Imaging and Drug Delivery. *Nano Res.* **2008**, *1*, 203−212.

(10) Ma, J.; Liu, R.; Wang, X.; Liu, Q.; Chen, Y.; Valle, R. P.; Zuo, Y. Y.; Xia, T.; Liu, S. Crucial Role of Lateral Size for Graphene Oxide in Activating Macrophages and Stimulating Pro-inflammatory Responses in Cells and Animals. *ACS Nano* **2015**, *9*, 10498−515.

(11) Alshamsan, A. Nanotechnology-Based Cancer Vaccine. *Methods Mol. Biol.* **2017**, *1530*, 257−270.

(12) Scheinberg, D. A.; McDevitt, M. R.; Dao, T.; Mulvey, J. J.; Feinberg, E.; Alidori, S. Carbon nanotubes as vaccine scaffolds. *Adv. Drug Delivery Rev.* **2013**, *65*, 2016−2022.

(13) Cunha-Matos, C. A.; Millington, O. R.; Wark, A. W.; Zagnoni, M. Real-time assessment of nanoparticle-mediated antigen delivery and cell response. *Lab Chip* **2016**, *16*, 3374−3381.

(14) Novoselov, K. S.; Geim, A. K.; Morozov, S. V.; Jiang, D.; Zhang, Y.; Dubonos, S. V.; Grigorieva, I. V.; Firsov, A. A. Electric field effect in atomically thin carbon films. *Science* **2004**, *306*, 666−669.

(15) Geim, A. K.; Novoselov, S. The rise of graphene. *Nat. Mater.* **2007**, *6*, 183−191.

(16) Hakimi, M.; Alimard, P. Graphene: synthesis and applications in biotechnology. *World Appl. Program* **2012**, *2*, 377−388.

(17) Liu, Z.; Robinson, J. T.; Sun, X.; Dai, H. PEGylated nanographene oxide for delivery of water insoluble cancer drugs. *J. Am. Chem. Soc.* **2008**, *130*, 10876−10877.

(18) Liao, K. H.; Lin, Y. S.; Macosko, C. W.; Haynes, C. L. Cytotoxicity of graphene oxide and graphene in human erythrocytes and skin fibroblasts. *ACS Appl. Mater. Interfaces* **2011**, *3*, 2607−2615.

(19) Zhang, X.; Yin, J.; Peng, C.; Hu, W.; Zhu, Z.; Li, W.; Fan, C.; Huang, Q. Distribution and biocompatibility studies of graphene oxide in mice after intravenous administration. *Carbon* **2011**, *49*, 986−995.

(20) Zhao, X.; Liu, L.; Li, X.; Zeng, J.; Jia, X.; Liu, P. Biocompatible graphene oxide nanoparticle based drug delivery platform for tumor microenvironment-responsive triggered release of doxorubicin. *Langmuir* **2014**, *30*, 10419−10429.

(21) Frost, R.; Jönsson, G. V.; Chakarov, D.; Svedhem, S.; Kasemo, B. Graphene oxide and lipid membranes: Interactions and nanocomposite structures. *Nano Lett.* **2012**, *12*, 3356−3362.

(22) Ip, A.C.-F.; Liu, B.; Huang, P.-J.; Liu, P. Oxidation level-dependent zwitterionic liposome adsorption and rupture by graphene-based materials and light-induced content release. *Small* **2013**, *9*, 1030−1035.

(23) Liu, X.; Chen, K. L. Interactions of graphene oxide with model cell membranes: Probing nanoparticle attachment and lipid bilayer disruption. *Langmuir* **2015**, *31*, 12076−12086.

(24) Wu, L.; Zeng, L.; Jiang, X. Revealing the nature of interaction between graphene oxide and lipid membrane by surface enhanced infrared absorption spectroscopy. *J. Am. Chem. Soc.* **2015**, *137*, 10052−10055.

(25) Liu, S. B.; Zeng, T. H.; Hofmann, M.; Burcombe, E.; Wei, J.; Jiang, R. R.; Kong, J.; Chen, Y. Antibacterial activity of graphite, graphite oxide, graphene oxide and reduced graphene oxide: membrane and oxidative stress. *ACS Nano* **2011**, *5*, 6971−6980.

(26) Cheng, C.; Nie, S.; Li, S.; Peng, H.; Yang, H.; Ma, L.; Sun, S.; Zhao, C. Biopolymer functionalized reduced graphene oxide with enhanced biocompatibility via mussel inspired coatings/anchors. *J. Mater. Chem. B* **2013**, *1*, 265−275.

(27) Nieva, J. L.; Goni, F. M.; Alonso, A. Liposome fusion catalytically induced by phospholipase C. *Biochemistry* **1989**, *28*, 7364−7367.

(28) Mastronarde, D. N. Automated electron microscope tomography using robust prediction of specimen movements. *J. Struct. Biol.* **2005**, *152*, 36−51.

(29) Kremer, J. R.; Mastronarde, D. N.; McIntosh, J. R. Computer visualization of three-dimensional image data using IMOD. *J. Struct. Biol.* **1996**, *116*, 71−76.

(30) Ellens, H.; Bentz, J.; Szoka, F. C. H^+- and Ca^{2+}-induced fusion and destabilization of liposomes. *Biochemistry* **1985**, *24*, 3099−3106.

(31) Gary-Bobo, C. M.; Solomon, A. K. Hemoglobin charge dependence on hemoglobin concentration in vitro. *J. Gen. Physiol.* **1971**, *57*, 283−289.

(32) Subirana, J. A.; Doty, P. Kinetics of renaturation of denatured DNA. I. spectrophotometric results. *Biopolymers* **1966**, *4*, 171−187.